Uromodulin is expressed in the distal convoluted tubule, where it is critical for regulation of the sodium chloride cotransporter NCC

Tokonami, Natsuko ; Takata, Tomoaki ; Beyeler, Jan ; Ehrbar, Iris ; Yoshifuji, Ayumi ; Christensen, Erik I ; Loffing, Johannes ; Devuyst, Olivier ; Olinger, Eric G

Abstract: Uromodulin, the most abundant protein in normal urine, is essentially produced by the cells lining the thick ascending limb. There it regulates the activity of the cotransporter NKCC2 and is involved in sodium chloride handling and blood pressure regulation. Conflicting reports suggested that uromodulin may also be expressed in the distal convoluted tubule (DCT) where its role remains unknown. Using microdissection studies combined with fluorescent in situ hybridization and co-immunostaining analyses, we found a significant expression of uromodulin in mouse and human DCT at approximately 10% of thick ascending limb expression levels, but restricted to the early part of the DCT (DCT1). Genetic deletion of Umod in mouse was reflected by a major shift in NCC activity from the DCT1 to the downstream DCT2 segment, paralleled by a compensatory expansion of DCT2. By increasing the distal sodium chloride and calcium ion load with chronic furosemide administration, an intrinsic compensatory defect in the DCT from Umod-/- compared to wild type mice was found manifested as sodium wasting and hypercalciuria. In line, co-expression studies in HEK cells suggested a facilitating role for uromodulin in NCC phosphorylation, possibly via SPAK-OSR1 modulation. These experiments demonstrate a significant expression of uromodulin in the early part of mouse and human DCT. Thus, biosynthesis of uromodulin in the DCT1 is critical for its function, structure and plasticity, suggesting novel links between uromodulin, blood pressure control and risk of kidney stones.

DOI: https://doi.org/10.1016/j.kint.2018.04.021

Uromodulin is expressed in the distal convoluted tubule, where it is critical for regulation of the sodium chloride cotransporter NCC

OPEN

Natsuko Tokonami[1,4], Tomoaki Takata[1,4], Jan Beyeler[1], Iris Ehrbar[1], Ayumi Yoshifuji[1], Erik I. Christensen[2], Johannes Loffing[3], Olivier Devuyst[1,5] and Eric G. Olinger[1,5]

[1]Institute of Physiology, University of Zurich, Zurich, Switzerland; [2]Department of Biomedicine, Aarhus University, Aarhus, Denmark; and [3]Institute of Anatomy, University of Zurich, Zurich, Switzerland

Uromodulin, the most abundant protein in normal urine, is essentially produced by the cells lining the thick ascending limb. There it regulates the activity of the cotransporter NKCC2 and is involved in sodium chloride handling and blood pressure regulation. Conflicting reports suggested that uromodulin may also be expressed in the distal convoluted tubule (DCT) where its role remains unknown. Using microdissection studies combined with fluorescent *in situ* hybridization and co-immunostaining analyses, we found a significant expression of uromodulin in mouse and human DCT at approximately 10% of thick ascending limb expression levels, but restricted to the early part of the DCT (DCT1). Genetic deletion of *Umod* in mouse was reflected by a major shift in NCC activity from the DCT1 to the downstream DCT2 segment, paralleled by a compensatory expansion of DCT2. By increasing the distal sodium chloride and calcium ion load with chronic furosemide administration, an intrinsic compensatory defect in the DCT from *Umod*$^{-/-}$ compared to wild type mice was found manifested as sodium wasting and hypercalciuria. In line, co-expression studies in HEK cells suggested a facilitating role for uromodulin in NCC phosphorylation, possibly via SPAK-OSR1 modulation. These experiments demonstrate a significant expression of uromodulin in the early part of mouse and human DCT. Thus, biosynthesis of uromodulin in the DCT1 is critical for its function, structure and plasticity, suggesting novel links between uromodulin, blood pressure control and risk of kidney stones.

Kidney International (2018) ■, ■–■; https://doi.org/10.1016/j.kint.2018.04.021

KEYWORDS: blood pressure regulation; distal convoluted tubule; Na^+/Cl^--cotransporter; salt handling; uromodulin

Correspondence: *Olivier Devuyst, University of Zurich, Institute of Physiology, Winterthurerstrasse 190, Zurich CH-8057, Switzerland. E-mail: olivier.devuyst@uzh.ch*

[4]These authors contributed equally to the study.

[5]OD and EGO co-directed and contributed equally to the study.

Received 13 January 2018; revised 3 April 2018; accepted 19 April 2018

Uromodulin, the most abundant protein in healthy urine, is exclusively expressed in the kidney,[1] with transcription levels among the highest in this organ.[2] Early studies in mammalian species, including humans, established that uromodulin is essentially synthesized in the epithelial cells lining the thick ascending limb (TAL) of the loop of Henle.[3,4] Uromodulin is a glycosylphosphatidylinositol–anchored protein targeted to the apical membrane, where it is cleaved by the serine protease hepsin. In the lumen, uromodulin monomers assemble via their zona pellucida domain to form a dense matrix of high-molecular-weight polymers constituting the hyaline casts.[5] The biological importance of uromodulin is supported by genetic evidence. Rare mutations in the *UMOD* gene encoding uromodulin lead to defective trafficking of mutant uromodulin, with endoplasmic reticulum (ER) stress causing autosomal dominant tubulointerstitial kidney disease.[6,7] Genome-wide association studies have revealed that common variants in the promoter of *UMOD* are associated with the risk of chronic kidney disease, calcium stones, and hypertension in the general population.[8–10]

The physiological roles of uromodulin, which have been demonstrated in *Umod*$^{-/-}$ mice, include protection against intrarenal/tubular calcium oxalate crystallization[11] and regulation of the activity and surface abundance of the $Na^+/K^+/2Cl^-$ cotransporter NKCC2, and renal outer medullary potassium channel ROMK in the TAL, hence the sodium avidity and urinary concentrating ability of the kidney.[12–14] The latter hypothesis is supported by the fact that the *UMOD* variants associated with hypertension drive higher uromodulin expression and are accompanied by higher NKCC2 activity in humans.[15]

If the TAL is established as the major site of uromodulin production, there are conflicting reports about a potential expression of uromodulin gene and protein in downstream segments. Radio-labeled *in situ* hybridization detected *Umod* mRNA signals in the rat TAL, with an abrupt ending at the transition to the distal convoluted tubule (DCT).[3] Consistent with this finding, immunofluorescent and electron microscopy in rat kidney detected uromodulin only in TAL cells, excepting the macula densa.[16,17] In contrast, uromodulin protein was reported in the DCT of hamster,[18] rat,[19] mouse,[20] and human[4] kidneys. However, these results were inconclusive because the positive immunostaining signal could reflect

luminal uromodulin adhering on the apical region of tubular cells lining segments downstream of the production site in the TAL. In fact, studies in human kidney showed that, in contrast to the plasmalemmal and cytoplasmic staining for uromodulin in TAL cells, only the very luminal plasmalemma was stained in DCT cells.[21] More recently, transcriptomic data showed some level of uromodulin mRNA in the DCT in mouse,[22] rat,[23] and human[24] kidneys—again difficult to interpret owing to potential contamination by the very high expression levels in adjacent TAL segments.

In this study we combined multilevel analyses of uromodulin mRNA and protein expression along the TAL and the DCT and in-depth testing of mouse models to demonstrate a specific expression of uromodulin in the early part of the DCT, with a distinct role in Na^+/Cl^- cotransporter (NCC) activation and local electrolyte handling.

RESULTS

Localization of *Umod* transcripts by microdissection in rodent kidney

We first analyzed the abundance of *Umod* transcripts by quantitative reverse transcription–polymerase chain reaction (RT-qPCR) using well-characterized tubular segments of mouse kidney obtained by microdissection.[25] The highest *Umod* transcript levels were detected in the TAL, followed by the DCT that showed ~10% of TAL expression levels (24.3 ± 3.4 vs. 2.1 ± 0.8 in DCT; expressed as $2^{\wedge}(Ct^{Gapdh}\text{-}Ct^{Umod}) \times 10^6$). *Umod* transcripts were undetectable in proximal tubules and collecting duct fractions (Figure 1a). We excluded TAL contamination in DCT fractions by showing virtual absence of *Slc12a1f* transcripts, encoding NKCC2F, the most abundant isoform expressed in the outer medulla (Figure 1b).[26]

We confirmed the presence of *Umod* transcripts in a pure DCT1 fraction by using fluorescence-assisted microdissection. The transgenic mouse line PV-EGFP expresses enhanced green fluorescence protein (EGFP) under the promoter of the *Pvalb* gene, encoding parvalbumin selectively in DCT1 cells.[27,28] Colocalization of EGFP with NCC confirmed its localization in DCT1 versus DCT2 segments (Figure 1*ci*, *ii*). Robust *Umod* transcript levels were detected in pure DCT1 fractions, characterized by virtually absent *Slc12a1* (NKCC2) transcripts and high levels of *Slc12a3* (NCC) transcripts (*Slc12a3*: 5.2 ± 0.6; *Umod*: 1.4 ± 0.3; *Slc12a1*: 0.001 ± 0.0003; expressed as

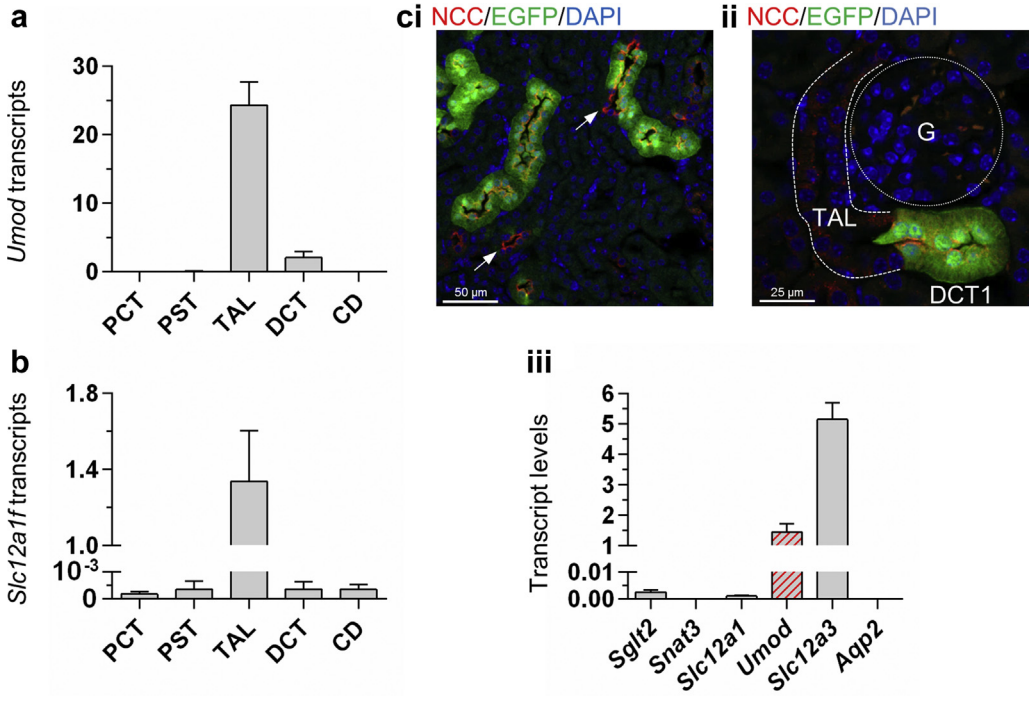

Figure 1 | Localization of *Umod* transcripts by microdissection in rodent kidney. (**a**) *Umod* transcript levels in microdissected kidney segments from C57BL/6J mice as assessed by quantitative reverse transcription–polymerase chain reaction (RT-qPCR). Levels are expressed as $2^{\wedge}(Ct^{Gapdh}\text{-}Ct^{Umod}) \times 10^{\wedge}6$. Bars indicate average ± SEM. n = 3 fractions. (**b**) *Slc12a1f* transcript levels in microdissected mouse kidney segments as assessed by RT-qPCR. Levels are expressed as $2^{\wedge}(Ct^{Gapdh}\text{-}Ct^{Slc12a1f}) \times 10^{\wedge}6$. Bars indicate average ± SEM. n = 3 fractions. (**c**) (***i***) Representative immunofluorescence staining of Na^+/Cl^- cotransporter (NCC, red) on paraffin-embedded kidney sections from PV-EGFP mice.[27,28] Arrows indicate NCC-positive, enhanced green fluorescence protein (EGFP)-negative segments. Nuclei are counterstained with 4′,6-diamidino-2-phenylindole (DAPI). (***ii***) Transition from a TAL segment (NCC-negative) to a DCT1 segment (NCC- and EGFP-positive) on a paraffin-embedded kidney section from a PV-EGFP mouse. Nuclei are counterstained with DAPI. (***iii***) Transcript levels of indicated genes in DCT1 fractions obtained by fluorescence-assisted microdissection on PV-EGFP kidneys. Levels are expressed as $2^{\wedge}(Ct^{Gapdh}\text{-}Ct^{target\ genes}) \times 10^{\wedge}6$. Bars indicate average ± SEM. n = 5 fractions. CD, collecting duct; DCT, distal convoluted tubule; G, glomerulus; PCT, proximal convoluted tubule; PST, proximal straight tubule; TAL, thick ascending limb. To optimize viewing of this image, please see the online version of this article at www.kidney-international.org.

$2^{\wedge}(Ct^{Gapdh}\text{-}Ct^{target\ gene}) \times 10^{\wedge}6$) (Figure 1c*iii*). Analysis of open-source transcriptomics databases confirmed that *Umod* transcripts in DCT accounted for 3.8% and 2.6% of cortical TAL levels in CD1 mice and Sprague-Dawley rats, respectively (Supplementary Figure S1A, B).[22,23]

Localization of *Umod* transcripts by *in situ* hybridization in mouse kidney

Multiplex fluorescent *in situ* hybridization probes were designed for *Umod, Slc12a1* (NKCC2), and *Slc12a3* (NCC), the specificity of the *Umod* probe being verified on $Umod^{-/-}$ kidneys (Supplementary Figure S2). Hybridization on mouse kidney revealed 2 clusters of *Umod*-positive tubules (green) in the cortex, differing in their amount of *Umod* dots (Figure 2a). The high *Umod* mRNA tubules (arrows) were positive for *Slc12a1* (red) and negative for *Slc12a3* (cyan), identifying them as TALs. In contrast, the low *Umod* mRNA tubules (arrowheads) were negative for *Slc12a1* (red) and positive for *Slc12a3* (cyan), identifying them as DCTs. No *Umod* mRNA expression outside of TAL or DCT was detected. The distinct *Umod* mRNA expression patterns are clearly visible in TAL (Figure 2b) and DCT (Figure 2c) segments, with an abrupt transition in *Umod* mRNA abundance from TAL to DCT1 (Figure 2d). Semi-automated quantification of fluorescent dots, representing single *Umod* mRNA molecules,[29] indicated that an average DCT tubule expresses ~15% of the *Umod* mRNA expressed in a cortical TAL (138.6 ± 8.0 vs. 20.8 ± 2.0 in DCT, arbitrary units representing dots normalized to tubule area) (Figure 2e). This finding is in close agreement with the expression values detected by RT-qPCR on microdissected tubules.

Umod expression in TAL along the corticomedullary axis

An increasing body of evidence suggests the TAL being heterogeneous along the corticomedullary axis.[30] Transcriptomics data suggested higher *Umod* expression in cortical TAL (cTAL) compared with medullary TAL (mTAL) in rodent kidney (1.4- and 7.8-fold higher expression in mouse and rat cTAL, respectively) (Supplementary Figure S1) and a trend in the same direction in human kidney.[24] Our analysis of mTAL and cTAL fractions, validated by enrichment of splicing isoforms of *Slc12a1* (Figure 3a), revealed 1.5-fold higher *Umod* transcript

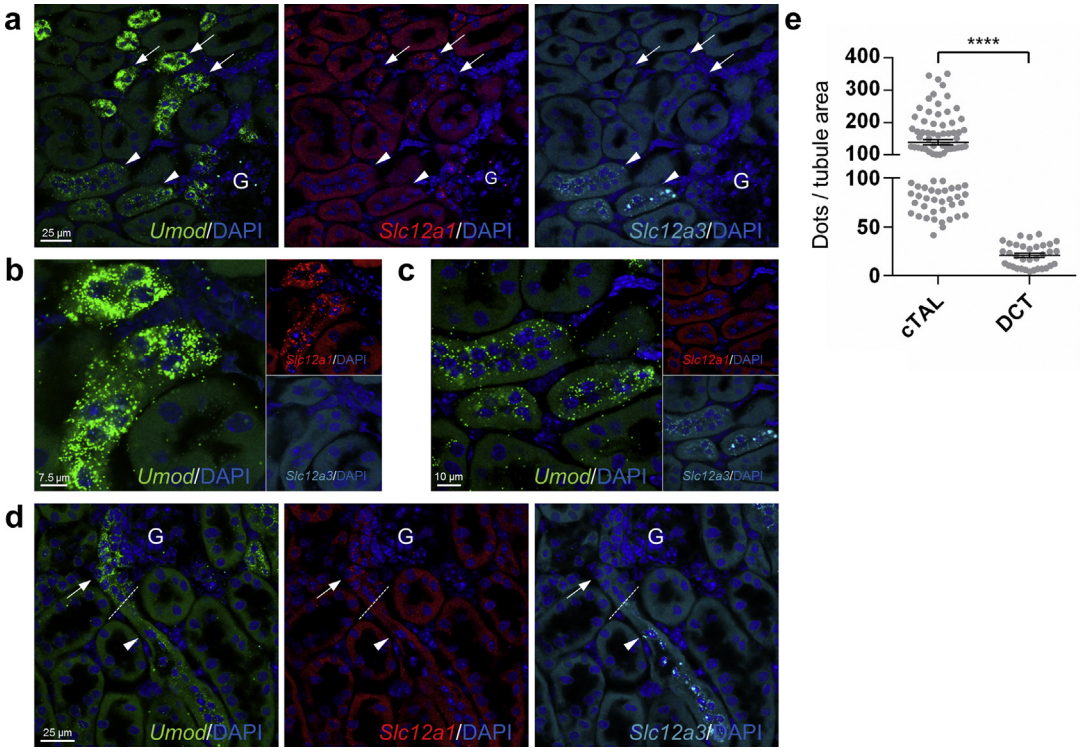

Figure 2 | Localization of *Umod* transcripts by *in situ* hybridization in mouse kidney. (**a**) Representative picture of fluorescent multiplex *in situ* hybridization (RNAscope) for *Umod* (green), *Slc12a1* (red), and *Slc12a3* (cyan) on cryosections from mouse kidney. *Umod* mRNA is consistently detected in distal convoluted tubule (DCT) tubules (arrowheads), albeit at lower levels compared with cortical thick ascending limb (cTAL) tubules (arrows). Nulcei are counterstained with 4′,6-diamidino-2-phenylindole (DAPI). (**b**) High-magnification fluorescent multiplex *in situ* hybridization showing *Umod* mRNA in cTAL, as identified by positive *Slc12a1* mRNA detection and absent *Slc12a3* mRNA. Nuclei are counterstained with DAPI. (**c**) High-magnification fluorescent multiplex *in situ* hybridization showing *Umod* mRNA in DCT, as identified by absent *Slc12a1* mRNA and detection of *Slc12a3* mRNA. Nulcei are counterstained with DAPI. (**d**) Fluorescent multiplex *in situ* hybridization showing *Umod* mRNA at the transition from cTAL (arrow) to DCT (arrowhead). Nuclei are counterstained with DAPI. (**e**) Semi-automated quantification of *Umod* mRNA dots (representing single mRNA molecules[29]) normalized to tubule area in cTAL tubules (n = 87) versus DCT tubules (n = 34); n = 2 mice. Bars represent mean ± SEM; ****$P < 0.0001$ (Unpaired 2-tailed *t* test). G, glomerulus. To optimize viewing of this image, please see the online version of this article at www.kidney-international.org.

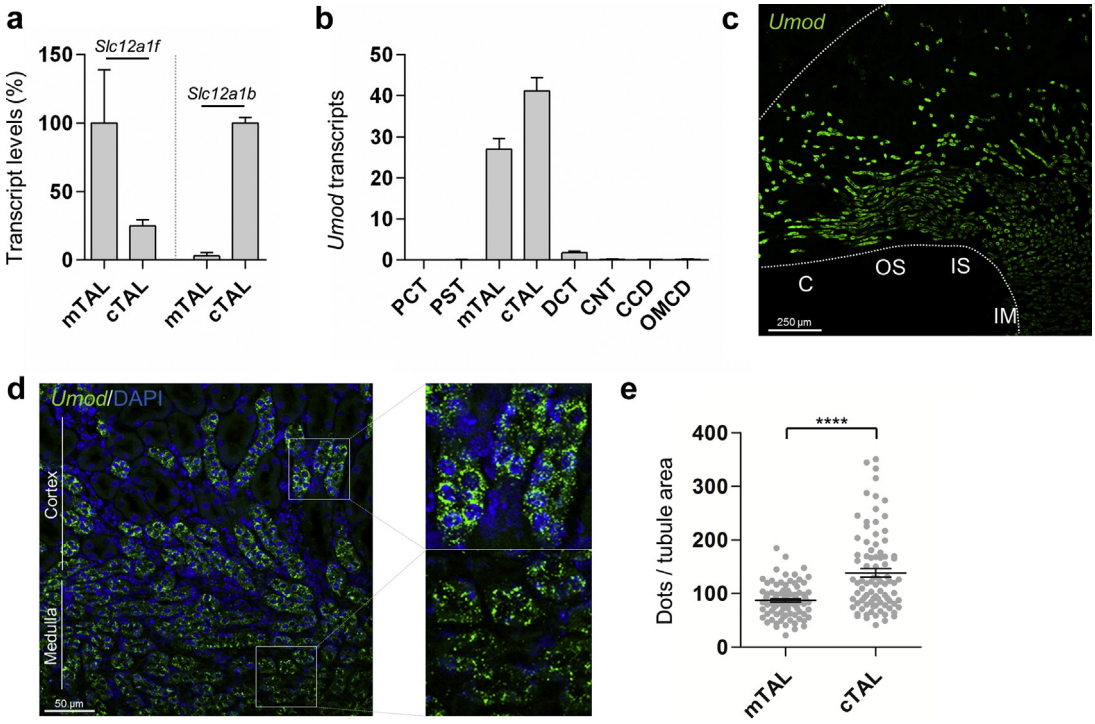

Figure 3 | *Umod* expression along the corticomedullary axis of the thick ascending limb (TAL). (**a**) Relative transcript levels of *Slc12a1f* and *Slc12a1b*, as assessed by quantitative reverse transcription–polymerase chain reaction (RT-qPCR) in medullary TAL (mTAL) and cortical TAL (cTAL) fractions isolated from mouse kidneys. Levels are expressed relative to corresponding enrichment marker. Bars indicate average ± SEM. n = 2 to 3 fractions. (**b**) *Umod* transcript levels in microdissected nephron segments from mouse kidneys as assessed by RT-qPCR. Levels are expressed as 2^(Ct^{Gapdh}-Ct^{Umod}) × 10^6. Bars indicate average ± SEM. n = 5 fractions. (**c**) Representative low-magnification fluorescent multiplex *in situ* hybridization (RNAscope) for *Umod* (green) on mouse kidney cryosections. Kidney borders indicated by white dashes. (**d**) Representative fluorescent multiplex *in situ* hybridization showing *Umod* mRNA in cTAL and mTAL on mouse kidney cryosections. Insets show higher magnifications of indicated cortical (upper panel) and medullary (lower panel) regions. Cortex is identified by the presence of glomeruli. Nuclei are counterstained with 4′,6-diamidino-2-phenylindole (DAPI). (**e**) Semi-automated quantification of *Umod* mRNA dots (representing single mRNA molecules[29]) normalized to tubule area in mTAL tubules (n = 90) versus cTAL tubules (n = 87). TAL tubules were identified by positive *Slc12a1* expression; cTAL identification required the presence of a glomerulus in the same high-magnification field. n = 2 mice. Bars indicate average ± SEM. ****$P < 0.0001$ (unpaired 2-tailed *t* test). C, cortex; CCD, cortical collecting duct; CNT, connecting tubule; DCT, distal convoluted tubule; IM, inner medulla; IS, inner stripe of the outer medulla; OMCD, outer medullary collecting duct; OS, outer stripe of the outer medulla; PCT, proximal convoluted tubule; PST, proximal straight tubule. To optimize viewing of this image, please see the online version of this article at www.kidney-international.org.

levels in the cTAL compared with mTAL (41.2 ± 3.2 vs. 27.0 ± 2.6 in mTAL, expressed as 2^(Ct^{Gapdh}-Ct^{Umod}) × 10^6) (Figure 3b). *In situ* hybridization showed a corticomedullary gradient for *Umod* expression, with cortical TALs displaying a stronger fluorescent labeling compared with mTALs (Figure 3c, d). Semi-automated quantification of fluorescent dots indicates that an average cTAL (as defined by close spatial relation with a glomerulus) expresses roughly 1.6-fold the amount of *Umod* mRNA expressed in mTAL (138.6 ± 8.0 vs. 87.2 ± 3.2 in mTAL, arbitrary units representing dots normalized to tubule area) (Figure 2e), similar to the RT-qPCR data.

Immunofluorescent localization of uromodulin along the DCT

To investigate whether the *Umod* mRNA expression in DCT is mirrored by uromodulin protein localization, we performed immunofluorescent stainings for uromodulin and NCC in serial sections from mouse kidneys (Figure 4a). A cluster of tubules displaying a signal for uromodulin (green) and for NCC (red; arrowheads) was identified (Figure 4a, upper panels). The uromodulin signal was weaker in the NCC-positive tubules (DCT) compared with that observed in TAL segments (Figure 4a, lower panels). Furthermore, a consistent uromodulin expression was detected in EGFP-expressing DCT1 tubules in sections from PV-EGFP mouse kidneys, with confirmation of different staining intensity between TAL and DCT segments (Figure 4b). Confocal imaging showed uromodulin located at the apical plasma membrane in DCT1 tubules (arrow), similar to the TAL distribution pattern (arrowhead) (Figure 4c). Coimmunostaining for uromodulin (green) and NCC (red) in human kidney confirmed the partial overlap of expression (arrow) (Figure 4d), in line with mRNA data.[24] Uromodulin was also detected by immunoperoxidase in parvalbumin-expressing human DCT1 (Figure 4e).

Because missense mutations in *UMOD* are causing an ER accumulation of mutant uromodulin in autosomal dominant tubulointerstitial kidney disease,[6,7] we assessed whether uromodulin is also accumulating inside the DCT of the *Umod*$^{C125R/+}$ mouse model.[7] Immunofluorescent analyses showed that, in addition to the TAL, uromodulin is

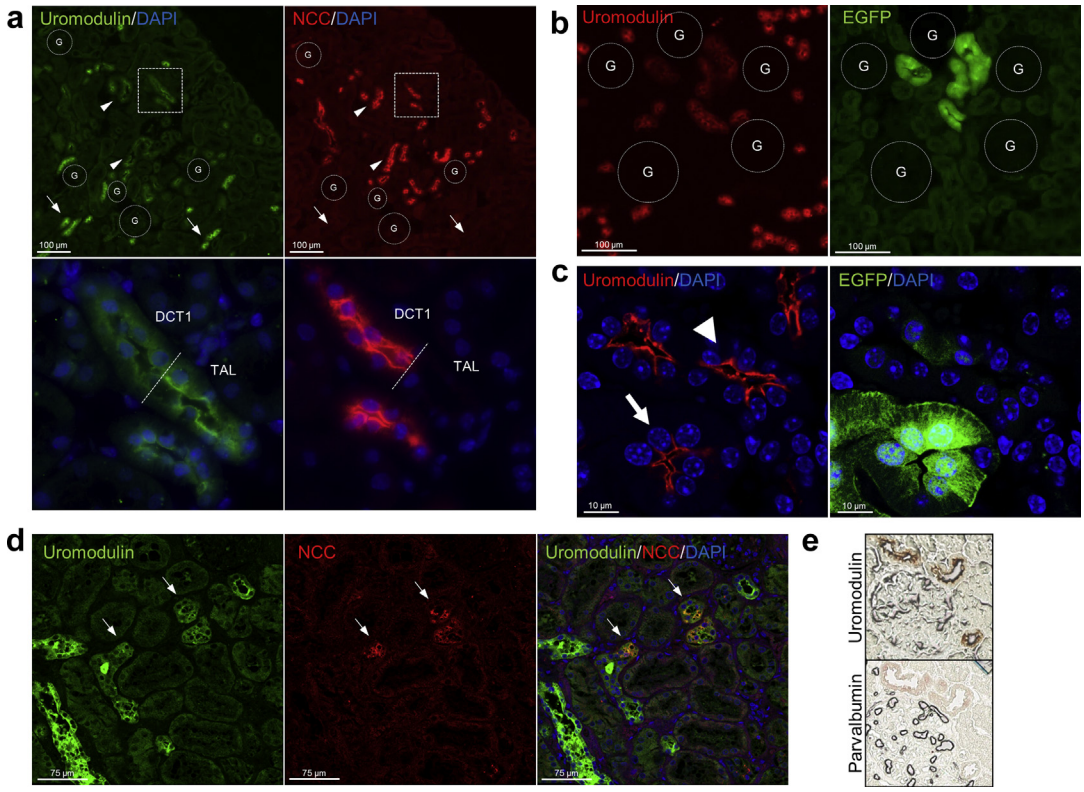

Figure 4 | Immunofluorescent localization of uromodulin along the distal convoluted tubule (DCT). (**a**) Upper panels: Representative immunofluorescence staining for uromodulin (green) and Na^+/Cl^- cotransporter (NCC, red) on serial paraffin-embedded sections from mouse kidney, showing consistent but weaker staining of uromodulin in NCC-positive tubules (arrowheads) compared with putative thick ascending limbs (TALs) (arrows). Lower panels: Higher magnification of a transition from a TAL to an NCC-positive DCT1 and highlighting the accompanying decrease in uromodulin intensity. Nuclei are counterstained with 4′,6-diamidino-2-phenylindole (DAPI). (**b**) Representative immunofluorescence staining for uromodulin (red) on paraffin-embedded kidney sections from PVALB-EGFP mice, confirming consistent but weaker staining of uromodulin in enhanced green fluorescent protein (EGFP, green) positive DCT1 tubules. (**c**) Apical localization of uromodulin (red) in DCT1, as shown on immunofluorescent confocal imaging on paraffin-embedded PVALB-EGFP kidneys (arrow). A putative TAL is shown for comparison (arrowhead). Nuclei are counterstained with DAPI. (**d**) Representative immunofluorescence staining for uromodulin (green) and NCC (red) on paraffin-embedded sections from normal human kidney showing partial overlap of signal (arrow). (**e**) Immunoperoxidase labeling for uromodulin and parvalbumin on normal human kidney serial sections showing partial overlap of signal in DCT1. (Continued)

accumulating in the cytoplasm of DCT cells in $Umod^{C125R/+}$ kidneys, contrasting with its apical expression in $Umod^{+/+}$ mice (Figure 4f). These data provide more evidence for the biosynthesis of uromodulin in the DCT.

Uromodulin expression is restricted to the DCT1 segment in mouse kidney

The DCT is divided into the functionally distinct DCT1 and downstream DCT2.[31,32] A cluster of tubules identified as DCT by *in situ* hybridization were devoid of *Umod* expression, whereas others showed consistent *Umod* expression (Figure 5a). Furthermore, some DCTs in the $Umod^{C125R/+}$ kidneys were not accumulating uromodulin (Figure 4f). To assess whether uromodulin expression is restricted to DCT1, we performed a triple staining with uromodulin (green), NCC (cyan), and parvalbumin (red) (Figure 5b). The DCT1 sections were defined as NCC- and parvalbumin-positive, whereas NCC-positive and parvalbumin-negative tubules were defined as DCT2. A strong expression gradient for uromodulin was quantified along the DCT, with DCT2 expression intensity being ~15% of that detected in DCT1 (DCT2: 14.9% ± 2.4% of DCT1 uromodulin expression, assessed as uromodulin fluorescent intensity normalized to tubule area) (Figure 5c). In line with this finding, fluorescent costaining analyses between uromodulin and TRPV5 (ECaC1), an apical Ca^{2+} channel expressed in the DCT2 and the downstream connecting tubule but not in DCT1,[32] showed no significant co-distribution (Figure 5d). These data show that a significant expression of uromodulin is also detected in the DCT, being largely restricted to the initial portion of that segment (DCT1). Uromodulin is not detected elsewhere than in the TAL and DCT.

Structural effects of uromodulin in mouse DCT

The DCT is critical for the transcellular reabsorption of NaCl, mediated by NCC, and the fine-tuning of urinary Ca^{2+} and Mg^{2+} excretion.[31] Absence of uromodulin in $Umod^{-/-}$ mice is known to affect apical transport systems in the TAL, causing adaptations in the DCT (i.e., NCC hyperactivation and DCT hypertrophy).[12] To substantiate our findings of uromodulin expression in DCT1, we dissected direct effects of uromodulin on DCT function from secondary compensatory

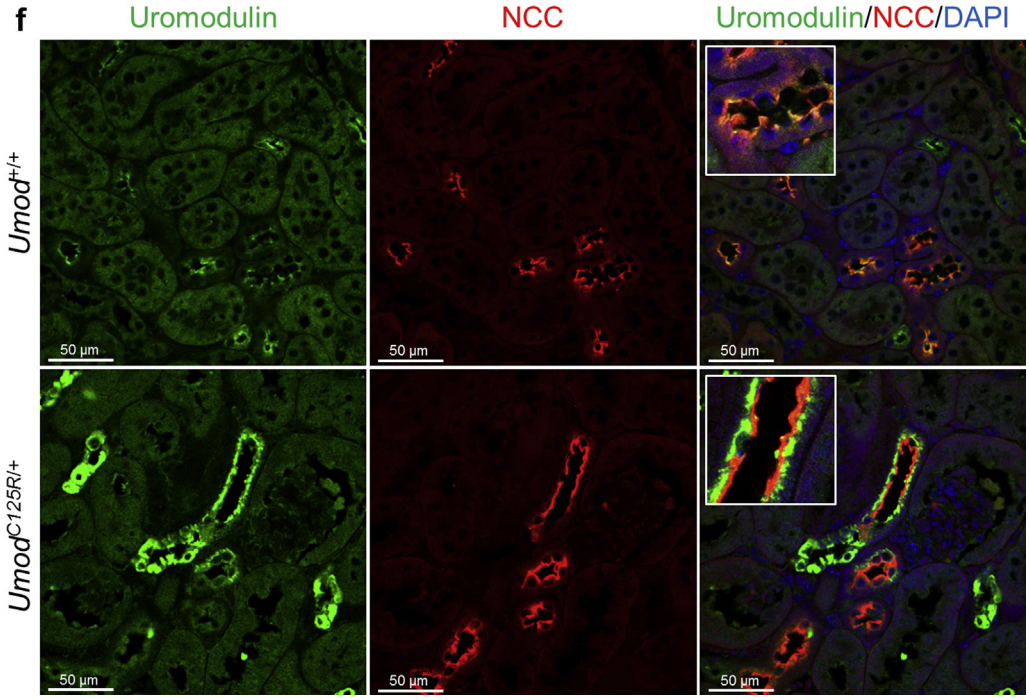

Figure 4 | (Continued) (**f**) Representative immunofluorescence staining for uromodulin (green) and NCC (red) on paraffin-embedded kidney sections from *Umod*$^{+/+}$ and *Umod*$^{C125R/+}$ mice. Nuclei are counterstained with DAPI. G, glomerulus. To optimize viewing of this image, please see the online version of this article at www.kidney-international.org.

mechanisms by using a chronic (5-day) furosemide treatment coupled with acute hydrochlorothiazide (HCTZ) administration in *Umod*$^{-/-}$ and *Umod*$^{+/+}$ mice.

At baseline, *Umod*$^{-/-}$ mice showed a slight increase in total NCC expression in total kidney membranes, in line with previous report.[12] The phosphorylated NCC (pNCC) (at T53 and T58) were both increased, reflecting ~1.5-fold increased pNCC/total NCC ratios in *Umod*$^{-/-}$ compared with *Umod*$^{+/+}$ mice (Figure 6a, b). Chronic furosemide infusion, which increases distal Na^+ delivery and triggers DCT activity,[33] led to a dramatic increase of total and phosphorylated NCC in both groups (+270% vs. 284% for total NCC; +978% vs. +1063% for T53 pNCC; and +685% vs. +675% for T58 pNCC in *Umod*$^{+/+}$ and *Umod*$^{-/-}$ mice, respectively, relative to *Umod*$^{+/+}$ baseline levels) (Figure 6a, b). Although the absolute levels of total NCC and pNCC were similar between the 2 genotypes after furosemide, the fold change of pNCC (between baseline and furosemide infusion) was markedly reduced in *Umod*$^{-/-}$ mice (Figure 6c).

Because uromodulin is mostly expressed in DCT1, we investigated the relative contribution of DCT1 versus DCT2 in the changes observed. Immunostaining revealed a ~2-fold decrease of T53 pNCC in DCT1 tubules of *Umod*$^{-/-}$ versus *Umod*$^{+/+}$ mice at baseline (14.0 ± 0.9 vs. 25.6 ± 1.2, respectively; $P < 0.0001$; arbitrary units of fluorescent intensity per tubule area), paralleled by stronger T53 pNCC in DCT2 (20.8 ± 0.9 vs. 14.6 ± 0.7 respectively; $P < 0.0001$) (Figure 6d [upper panels] and Figure 6e [left panels]). Chronic furosemide infusion equalized the T53 pNCC signals in the DCT1 (28.1 ± 1.4 vs. 29.9 ± 1.4, respectively), whereas T53 pNCC was further increased in DCT2 of *Umod*$^{-/-}$ versus *Umod*$^{+/+}$ mice (33.4 ± 1.8 vs. 18.6 ± 1.7, respectively; $P < 0.0001$) (Figure 6d [lower panels] and Figure 6e [right panels]).

To detect structural adaptations, we investigated the renal fractional volume occupied by T53 pNCC-positive DCT1 versus DCT2 segments (Supplementary Figure S3).[34] At baseline the renal fractional volume occupied by pNCC-positive DCT1 was slightly lower in *Umod*$^{-/-}$ versus *Umod*$^{+/+}$ mice (1.6% ± 0.2% vs. 2.0% ± 0.2% of renal volume, respectively; $P = 0.09$). Conversely, the renal fractional volume occupied by pNCC-positive DCT2 was higher in *Umod*$^{-/-}$ versus *Umod*$^{+/+}$ mice (3.5% ± 0.4% vs. 1.5% ± 0.2% of renal volume, respectively; $P< 0.001$) (Figure 6f, left panels), in line with quantification data based on TRPV5 stainings (Supplementary Figure S4B). After chronic furosemide infusion, the renal fractional volume occupied by pNCC-positive DCT1 was significantly lower in *Umod*$^{-/-}$ versus *Umod*$^{+/+}$ mice (2.1% ± 0.3% vs. 3.2 ± 0.3% of renal volume, respectively; $P = 0.015$), whereas the renal fractional volume occupied by pNCC-positive DCT2 was higher (3.7% ± 0.3% vs. 2.5% ± 0.4% of renal volume, respectively; $P = 0.025$) (Figure 6f, right panel), also in line with TRPV5 staining data (Supplementary Figure S4B). Although chronic furosemide infusion triggers a significant compensatory increase in DCT1 and DCT2 fractional volume in *Umod*$^{+/+}$ mice, this response is markedly blunted in *Umod*$^{-/-}$ mice (Figure 6f, right panel; Supplementary Figure S4).

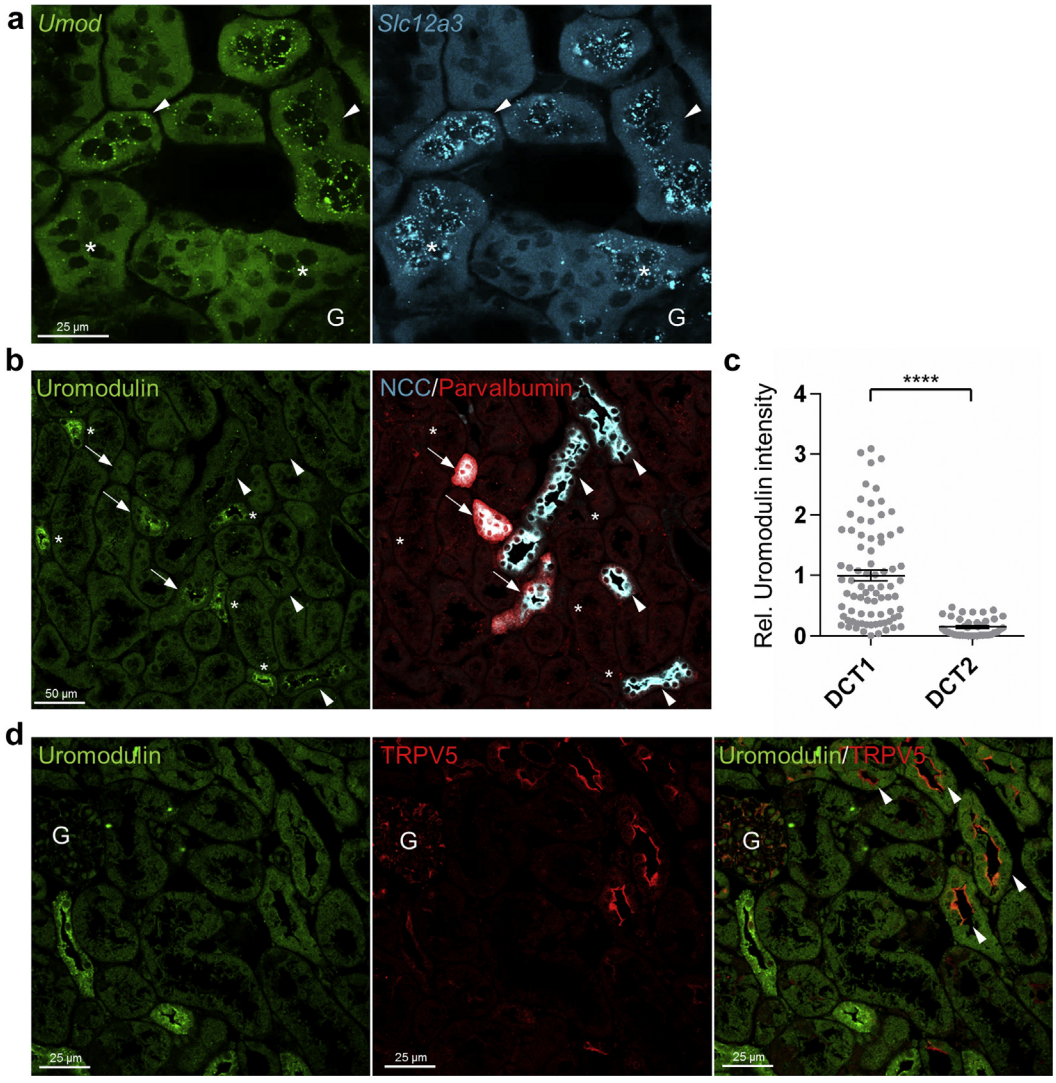

Figure 5 | Uromodulin expression is restricted to the early distal convoluted tubule (DCT1) segment. (**a**) Representative picture of fluorescent multiplex *in situ* hybridization (RNAscope) for *Umod* (green) and *Slc12a3* (cyan) on mouse kidney cryosections. A cluster of DCTs expressing *Slc12a3* is devoid of *Umod* mRNA (asterisk), in contrast to others abundantly expressing *Umod* (arrowheads). (**b**) Representative triple immunofluorescence staining for uromodulin (green), Na^+/Cl^- cotransporter (NCC, cyan), and parvalbumin (red) on paraffin-embedded kidney section showing segments of thick ascending limb (TAL) (asterisk), DCT1 (arrows), and DCT2 (arrowheads). (**c**) Quantification of uromodulin signal intensity in DCT1 and DCT2. The quantification is based on 79 DCT1 and 39 DCT2 segments from 15 distinct fields from 3 different mice. Results are expressed in arbitrary units representing uromodulin fluorescent intensity normalized to tubule area and to DCT1. Bars indicate average ± SEM. n = 3 mice. ****$P < 0.0001$ (unpaired 2-tailed *t* test). (**d**) Representative immunofluorescence staining for uromodulin (green) and TRPV5 (ECaC1, red) on paraffin-embedded kidney section, showing segments of DCT2/connecting tubule with absent uromodulin expression (arrowheads). G, glomerulus. To optimize viewing of this image, please see the online version of this article at www.kidney-international.org.

Functional effects of uromodulin in the mouse DCT

To test the DCT function at baseline and in the situation of increased NaCl delivery, we monitored NaCl, as well as Ca^{2+} and Mg^{2+} handling, after acute HCTZ injection at baseline and after chronic furosemide treatment in mice. The parameters of $Umod^{-/-}$ and $Umod^{+/+}$ mice were similar at baseline or after vehicle (0.9% NaCl) injection (Tables 1 and 2; Supplementary Table S1). Chronic furosemide infusion led to a slight urinary Na^+ wasting in $Umod^{-/-}$ but not in $Umod^{+/+}$ mice (Figure 7a*i*, Table 2; Supplementary Figure S5A), suggesting impaired distal tubular compensatory mechanisms. Acute HCTZ administration led to an exaggerated natriuretic response in $Umod^{-/-}$ mice, confirming NCC hyperactivation (Figure 7a*ii*, Table 1). HCTZ injection after the 5-day furosemide infusion revealed a significantly attenuated natriuretic response in $Umod^{-/-}$ versus $Umod^{+/+}$ mice (Figure 7a*ii*, Table 3), more evident when considering the fold change in HCTZ-induced natriuria between furosemide-infusion and control conditions (Figure 7a*iii*).

Chronic furosemide infusion yielded excessive urinary calcium wasting in $Umod^{-/-}$ versus $Umod^{+/+}$ mice, evident after 3–5 days of treatment (Figure 7b*i*, Table 2) and also

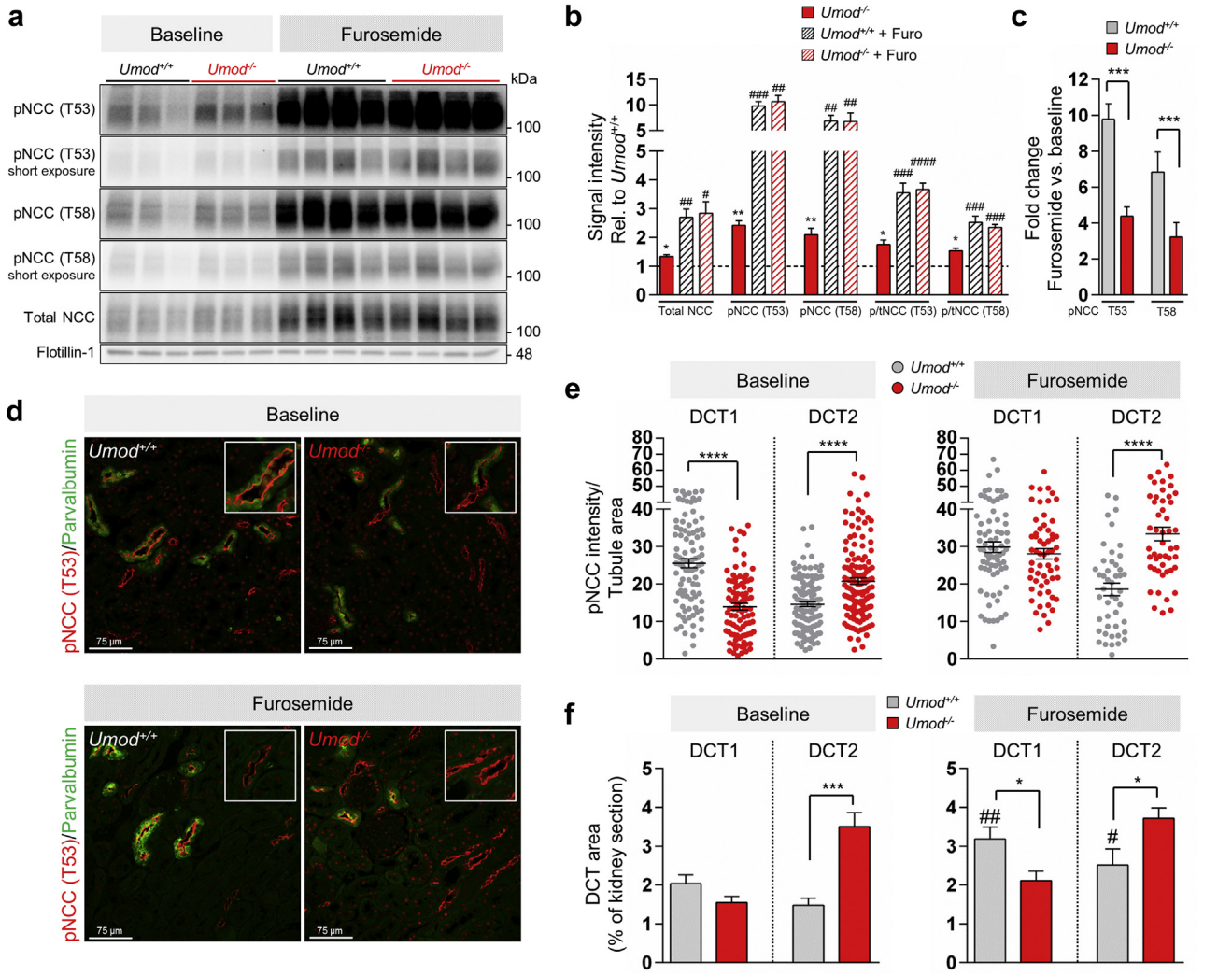

Figure 6 | Structural effects of uromodulin in the mouse distal convoluted tubule (DCT). (**a**) Western blot analysis for indicated (phospho)-proteins on kidney membrane fractions from *Umod*$^{+/+}$ and *Umod*$^{-/-}$ mice, at baseline or after 5-day furosemide infusion (75 µg/g body weight [gBW]/d). Short and long exposure times are shown, as indicated. Flotillin-1 is shown as a loading control. (**b**) Quantification of Western blot signal intensities, relative to expression in *Umod*$^{+/+}$ at baseline. Bars indicate average ± SEM. Unpaired 2-tailed *t* test, *Umod*$^{-/-}$ versus *Umod*$^{+/+}$: $^{*}P < 0.05$; $^{**}P < 0.01$; unpaired 2-tailed *t* test at baseline versus after furosemide (Furo): $^{\#}P < 0.05$; $^{\#\#}P < 0.01$; $^{\#\#\#}P < 0.001$; $^{\#\#\#\#}P < 0.0001$. (**c**) Quantification of Western blot signal intensities, in fold increase of phosphorylated NCC (pNCC) signal between baseline and furosemide infusion in *Umod*$^{+/+}$ and *Umod*$^{-/-}$ mice. Bars indicate average ± SEM. Unpaired 2-tailed *t* test, *Umod*$^{-/-}$ versus *Umod*$^{+/+}$: $^{***}P < 0.001$. (**d**) Representative immunofluorescence staining for T53 pNCC (red) and parvalbumin (green) on paraffin-embedded kidney sections from *Umod*$^{+/+}$ and *Umod*$^{-/-}$ mice, at baseline or after 5-day furosemide infusion (75 µg/gBW/d). Insets show zoom-ins on single tubules. (**e**) Quantification of T53 pNCC signal intensity in DCT1 (parvalbumin-positive) and DCT2 (parvalbumin-negative) segments from *Umod*$^{+/+}$ and *Umod*$^{-/-}$ mice, at baseline or after 5-day furosemide infusion (75 µg/gBW/d). Each parameter was quantified from at least 5 microscopic fields from at least 3 mice per genotype (at least 15 fields per genotype). Results are expressed in arbitrary units representing uromodulin fluorescent intensity normalized to tubule area. Each dot represents a tubule. Bars indicate average ± SEM. Unpaired 2-tailed *t* test. *Umod*$^{-/-}$ versus *Umod*$^{+/+}$: $^{****}P < 0.0001$. (**f**) Left panel: Renal fractional volume (% of total kidney section) occupied by DCT1 or DCT2 segments, as identified by positive T53 pNCC and positive or negative parvalbumine staining, respectively, in *Umod*$^{+/+}$ and *Umod*$^{-/-}$ mice, at baseline. Bars indicate average ± SEM. n = 9 low-magnification fields from 3 mice. Unpaired 2-tailed *t* test *Umod*$^{-/-}$ versus *Umod*$^{+/+}$: $^{***}P < 0.001$. Right panel: Renal fractional volume (% of total kidney section) occupied by DCT1 or DCT2 segments, as identified by positive T53 pNCC and positive or negative parvalbumine staining, respectively, in *Umod*$^{+/+}$ and *Umod*$^{-/-}$ mice, after a 5-day furosemide infusion (75 µg/gBW/d). Bars indicate average ± SEM. n = 9 low-magnification fields from 3 mice. Unpaired 2-tailed *t* test *Umod*$^{-/-}$ versus *Umod*$^{+/+}$: $^{*}P < 0.05$; unpaired 2-tailed *t* test at baseline versus after furosemide: $^{\#}P < 0.05$; $^{\#\#}P < 0.01$. To optimize viewing of this image, please see the online version of this article at www.kidney-international.org.

revealed by day-5 versus day-1 comparisons (Supplementary Figure S5B). Because the rate-limiting step for transcellular Ca^{2+} uptake in the DCT2 is the Ca^{2+} channel TRPV5, we investigated potential differences in its expression levels. Similar levels of apical TRPV5 were observed in both *Umod*$^{+/+}$ and *Umod*$^{-/-}$ kidneys, both at baseline and after furosemide infusion (Supplementary Figure S5C,D). Acute HCTZ injection reduced calciuria to a similar degree, whereas HCTZ treatment after furosemide infusion yielded a similar response in both genotypes (Figure 7b*ii*, Tables 1 and 3). Urinary

Table 1 | Urine and physiological parameters in *Umod*$^{-/-}$ and *Umod*$^{+/+}$ mice after acute hydrochlorothiazide (HCTZ) treatment

Parameter	Control			HCTZ		
	Umod$^{+/+}$	*Umod*$^{-/-}$	n	*Umod*$^{+/+}$	*Umod*$^{-/-}$	n
Body weight (BW; g)	30.1 ± 0.5	29.9 ± 1.1	5/5	29.6 ± 0.5	29.1 ± 0.8	5/5
Water intake (µl/min*gBW)	0.147 ± 0.012	0.150 ± 0.019	5/5	0.154 ± 0.011	0.135 ± 0.022	5/5
Diuresis (µl/min*gBW)	0.057 ± 0.031	0.061 ± 0.010	5/5	0.065 ± 0.006	0.103 ± 0.019	5/5
Urinary Na^+ (mol/mol creat)	28.8 ± 1.2	27.3 ± 2.5	5/5	35.9 ± 5.0	50.1 ± 2.9$^{\#\#*}$	5/5
Urinary Cl^- (mol/mol creat)	48.8 ± 2.8	54.5 ± 4.0	5/5	53.9 ± 6.5	72.1 ± 2.7$^{\#*}$	5/5
Urinary K^+ (mol/mol creat)	71.6 ± 2.6	78.8 ± 8.2	5/5	67.3 ± 4.7	75.3 ± 3.3	5/5
Urinary Ca^{2+} (mol/mol creat)	0.63 ± 0.14	0.59 ± 0.15	5/5	0.27 ± 0.03	0.38 ± 0.04	5/5
Urinary Mg^{2+} (mol/mol creat)	4.8 ± 0.2	4.9 ± 0.7	5/5	4.4 ± 0.4	5.3 ± 0.2	5/5

creat, creatinine; HCTZ, hydrochlorothiazide; n, number of mice (male, 3 months).
Values represent means ± SEM. Control: 0.9% NaCl 10 µl/g body weight (gBW), i.p., 6-hour urine collection; HCTZ: hydrochlorothiazide 50 µg/gBW, i.p., 6-hour urine collection.
Unpaired 2-tailed *t* test, *Umod*$^{-/-}$ versus *Umod*$^{+/+}$: $^{*}P < 0.05$.
Paired 2-tailed *t* test, control versus HCTZ: $^{\#}P < 0.05$; $^{\#\#}P < 0.01$.

magnesium excretion was similar in both genotypes, both at baseline and after acute HCTZ and chronic furosemide administration (Tables 1 and 2). Taken together, the functional tests support a specific role for uromodulin in the DCT, as chiefly evidenced by a defective response to furosemide-induced increase in NaCl delivery.

Uromodulin facilitates NCC phosphorylation *in vitro*

To investigate the effects of uromodulin on NCC phosphorylation, we used human embryonic kidney (HEK) cells stably expressing human uromodulin (hUMOD).[35] Transient transfection of human NCC in these hUMOD-expressing HEK cells and control HEK cells resulted in NCC protein expression, as shown by specific bands at the expected molecular weight of ~130 kDa above an aspecific band at 100 kDa, which is also present in mock-transfected cell lysates (Figure 8a). Analysis of the ratio of phosphorylated (at T55 and T60, corresponding to mouse T53 and T58) versus total NCC revealed a marked increase of the phosphorylated NCC in hUMOD-expressing HEK cells compared with control HEK cells (Figure 8b, c), suggesting a facilitating effect of uromodulin on NCC maturation and phosphorylation *in vitro*.

Phosphorylation of NCC is mediated by the WNK-SPAK/OSR1 pathway.[36] Immunoblotting of total kidney extracts revealed reduced levels of pSPAK/pOSR1 in *Umod*$^{-/-}$ versus *Umod*$^{+/+}$ mice (Supplementary Figure S6A–C). Immunostaining for pSPAK/pOSR1 was detected in DCT1 segments in *Umod*$^{+/+}$ kidneys, contrasting with a sharp transition and nearly undetectable signal in the DCT1 segments in *Umod*$^{-/-}$ kidneys (Supplementary Figure S6D).

DISCUSSION

Our studies demonstrate that uromodulin is expressed in the initial part of the distal convoluted tube (DCT1) in mouse and human kidney, along with peak levels in the cortical TAL. We show that the lack of uromodulin is associated with decreased pNCC in the DCT1, compensated by a stonger and broader expression of pNCC in the DCT2, suggesting a shift of NaCl uptake from DCT1 to downstream DCT2. The functional relevance of these changes in the DCT is further evidenced during chronic furosemide administration: increased distal delivery of NaCl and Ca^{2+} leads to sodium wasting and uncompensated hypercalciuria in *Umod*$^{-/-}$ mice compared with *Umod*$^{+/+}$ mice. These results suggest that the biosynthesis of uromodulin is relevant for the role of the DCT in NaCl and calcium homeostasis.

On the basis of its biochemical properties and capacity to form a hydrophobic gel-like structure, uromodulin has been associated for decades with the watertight property of the TAL

Table 2 | Urine and physiological parameters in *Umod*$^{-/-}$ and *Umod*$^{+/+}$ mice after chronic furosemide treatment

Parameter	Baseline			Chronic furosemide		
	Umod$^{+/+}$	*Umod*$^{-/-}$	n	*Umod*$^{+/+}$	*Umod*$^{-/-}$	n
Body weight (BW; g)	25.4 ± 1.2	27.6 ± 0.6	8/8	26.2 ± 0.7	28.4 ± 0.4$^{\#*}$	4/4
Water intake (µl/min*gBW)	0.146 ± 0.010	0.159 ± 0.008	8/8	0.244 ± 0.010$^{\#\#}$	0.368 ± 0.017$^{\#\#***}$	4/4
Diuresis (µl/min*gBW)	0.069 ± 0.003	0.072 ± 0.006	5/5	0.126 ± 0.015$^{\#}$	0.213 ± 0.035$^{\#}$	4/4
Urinary Na^+ (mol/mol creat)	26.4 ± 3.1	21.1 ± 1.0	8/8	28.8 ± 1.0	33.9 ± 3.7$^{\#}$	4/4
Urinary Cl^- (mol/mol creat)	49.7 ± 3.4	44.5 ± 2.8	8/8	45.5 ± 0.7	48.5 ± 3.6	4/4
Urinary K^+ (mol/mol creat)	74.0 ± 5.0	68.6 ± 3.2	8/8	74.9 ± 2.3	77.0 ± 3.8$^{\#}$	4/4
Urinary Ca^{2+} (mol/mol creat)	0.32 ± 0.04	0.26 ± 0.03	8/8	0.76 ± 0.04$^{\#\#\#}$	1.36 ± 0.13$^{\#\#**}$	4/4
Urinary Mg^{2+} (mol/mol creat)	4.1 ± 0.1	4.2 ± 0.1	8/8	5.6 ± 0.3$^{\#\#}$	5.5 ± 0.2$^{\#}$	4/4

Creat, creatinine; n, number of mice (males, 3 months).
Values represent means ± SEM. Baseline: average of two 16-hour overnight urine collections. Chronic furosemide: 75 µg/gBW/d for 5 days. Day-5 data are reported.
Unpaired 2-tailed *t* test, *Umod*$^{-/-}$ versus *Umod*$^{+/+}$: $^{*}P < 0.05$; $^{**}P < 0.01$; $^{***}P < 0.001$.
Paired 2-tailed *t* test, baseline versus furosemide day 5: $^{\#}P < 0.05$; $^{\#\#}P < 0.01$; $^{\#\#\#}P < 0.001$.

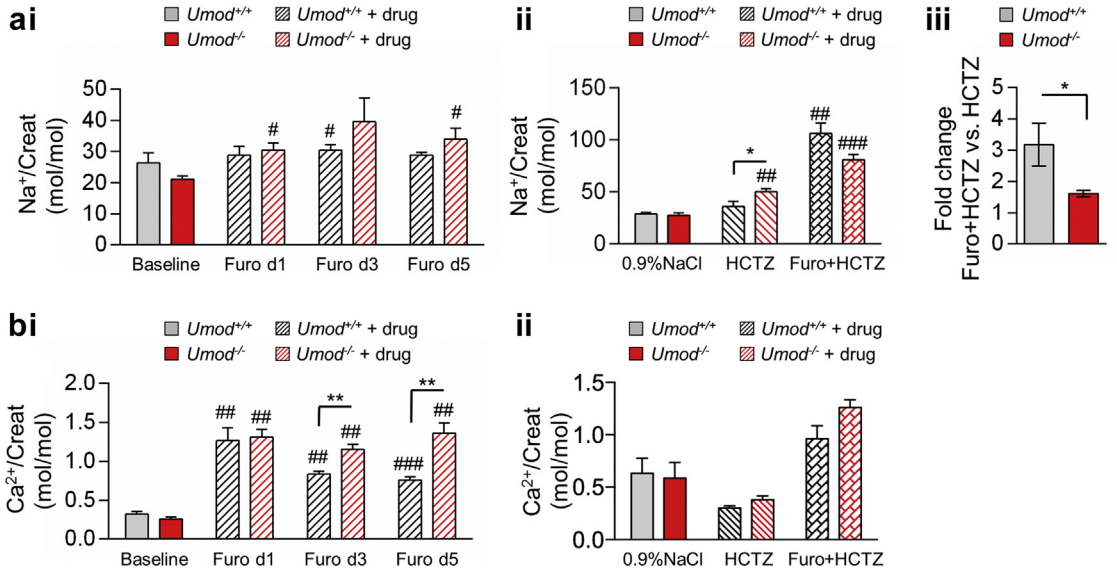

Figure 7 | Functional effects of uromodulin in the mouse DCT. (**a**) Urinary sodium/creatinine (Na^+/Creat) at baseline and after functional testing: (***i***) Evolution of urinary Na^+/Creat (mol/mol) from baseline to day 1, day 3, and day 5 of furosemide (Furo) infusion (75 μg/g body weight [gBW]/d) in *Umod*$^{-/-}$ and *Umod*$^{+/+}$ mice. Bars indicate average ± SEM. n = 8 at baseline and 4 during furosemide treatment. Paired 2-tailed *t* test baseline versus furosemide infusion: $^{\#}P < 0.05$. (***ii***) Urinary Na^+/Creat (mol/mol) after i.p. injection of 0.9% NaCl versus a single i.p. injection of 50 μg/gBW hydrochlorothiazide (HCTZ) in untreated mice or after 5 days of furosemide infusion in *Umod*$^{-/-}$ and *Umod*$^{+/+}$ mice, as indicated. Bars indicate average ± SEM. n = 5. Paired 2-tailed *t* test HCTZ versus control or furosemide infusion plus HCTZ versus furosemide infusion: $^{\#\#}P < 0.01$; $^{\#\#\#}P < 0.001$; unpaired 2-tailed *t* test *Umod*$^{-/-}$ versus *Umod*$^{+/+}$: *P ≤ 0.05. (***iii***) Fold change in urinary Na^+/Creat (mol/mol) after a single i.p. injection of 50 μg/gBW HCTZ in day-5 furosemide-infused *Umod*$^{-/-}$ and *Umod*$^{+/+}$ mice versus a single i.p. injection of 50 μg/gBW HCTZ in untreated mice. Bars indicate average ± SEM. Unpaired 2-tailed *t* test. *Umod*$^{-/-}$ versus *Umod*$^{+/+}$: $^{*}P < 0.05$. (**b**) Urinary calcium/creatinine (Ca^{2+}/Creat) at baseline and after functional testing: (***i***) Evolution of urinary Ca^{2+}/Creat (mol/mol) from baseline to day 1, day 3, and day 5 of furosemide infusion (75 μg/gBW/d) in *Umod*$^{-/-}$ and *Umod*$^{+/+}$ mice. Bars indicate average ± SEM. n = 8 at baseline and 4 during furosemide treatment. Paired 2-tailed *t* test, baseline versus furosemide-infusion: $^{\#\#}P < 0.01$; $^{\#\#\#}P < 0.001$; unpaired 2-tailed *t* test, *Umod*$^{-/-}$ versus *Umod*$^{+/+}$: $^{**}P < 0.01$. (***ii***) Urinary Ca^{2+}/Creat (mol/mol) after i.p. injection of 0.9% NaCl, after a single i.p. injection of 50 μg/gBW HCTZ in untreated mice or after 5 days of furosemide infusion in *Umod*$^{-/-}$ and *Umod*$^{+/+}$ mice. Bars indicate average ± SEM. n = 5.

and the urinary concentrating ability of the placental mammals.[5,37] Our finding of highest *Umod* expression in the cortical TAL, confirming previous reports,[3,22,23] and the robust expression of *Umod* in the DCT1 is at odds with a primary role of uromodulin in establishing and/or conserving the medullary osmolarity gradient. Considering the remarkable abundance of uromodulin transcripts, which correspond to ~5% of the poly(A)+ mRNA from human kidney[1] and to ~5% of the total rat cTAL transcriptome,[23] the levels of uromodulin expression detected in DCT1—corresponding to 10%–15% of that in the TAL—are far from being negligible. The expression pattern of uromodulin (cTAL > mTAL > DCT1) is likely to reflect specific functions in these specialized epithelia, complementing its role in the lumen.

Because the DCT reabsorbs NaCl and divalent cations,[31] it is tempting to speculate that uromodulin may play a role in these processes. Previous studies were inconclusive for a direct role of uromodulin in DCT, because baseline studies

Table 3 | Urine and physiological parameters in *Umod*$^{-/-}$ and *Umod*$^{+/+}$ mice after the acute addition of hydrochlorothiazide to chronic furosemide treatment

	Chronic furosemide			Chronic furosemide + HCTZ		
Parameter	*Umod*$^{+/+}$	*Umod*$^{-/-}$	n	*Umod*$^{+/+}$	*Umod*$^{-/-}$	n
Body weight (BW; g)	29.9 ± 0.6	31.6 ± 1.0	5/5	30.5 ± 0.5	29.6 ± 1.3	5/5
Water intake (μl/min*gBW)	0.240 ± 0.019	0.266 ± 0.021	5/5	0.306 ± 0.027	0.315 ± 0.035	5/5
Diuresis (μl/min*gBW)	0.148 ± 0.010	0.150 ± 0.014	5/5	0.224 ± 0.015$^{\#\#}$	0.214 ± 0.019	5/5
Urinary Na^+ (mol/mol creat)	21.9 ± 1.3	27.1 ± 2.2	5/5	106.2 ± 10.2$^{\#\#}$	80.9 ± 4.9$^{\#\#\#}$	5/5
Urinary Cl^- (mol/mol creat)	34.4 ± 2.7	44.4 ± 1.9*	5/5	116.7 ± 7.0$^{\#\#\#}$	99.1 ± 5.9$^{\#\#}$	5/5
Urinary K^+ (mol/mol creat)	57.9 ± 2.3	68.9 ± 3.7*	5/5	73.5 ± 3.1$^{\#\#\#}$	78.0 ± 0.8	5/5
Urinary Ca^{2+} (mol/mol creat)	0.86 ± 0.07	1.05 ± 0.04*	5/5	0.96 ± 0.12	1.26 ± 0.07	5/5
Urinary Mg^{2+} (mol/mol creat)	5.3 ± 0.2	5.5 ± 0.1	5/5	4.4 ± 0.4$^{\#\#}$	5.2 ± 0.3	5/5

HCTZ, hydrochlorothiazide; creat, creatinine; n, number of mice (male, 3 months).
Values represent means ± SEM. Chronic furosemide: 75 μg/gBW/d during 5 days; day-5 data are reported. Chronic furosemide plus HCTZ: HCTZ 50 μg/gBW, i.p., administered on day 5 of chronic furosemide, 6-hour urine collection.
Unpaired 2-tailed *t* test, *Umod*$^{-/-}$ versus *Umod*$^{+/+}$: $^{*}P < 0.05$.
Paired 2-tailed *t* test chronic furosemide versus chronic furosemide plus HCTZ: $^{\#\#}P < 0.01$; $^{\#\#\#}P < 0.001$.

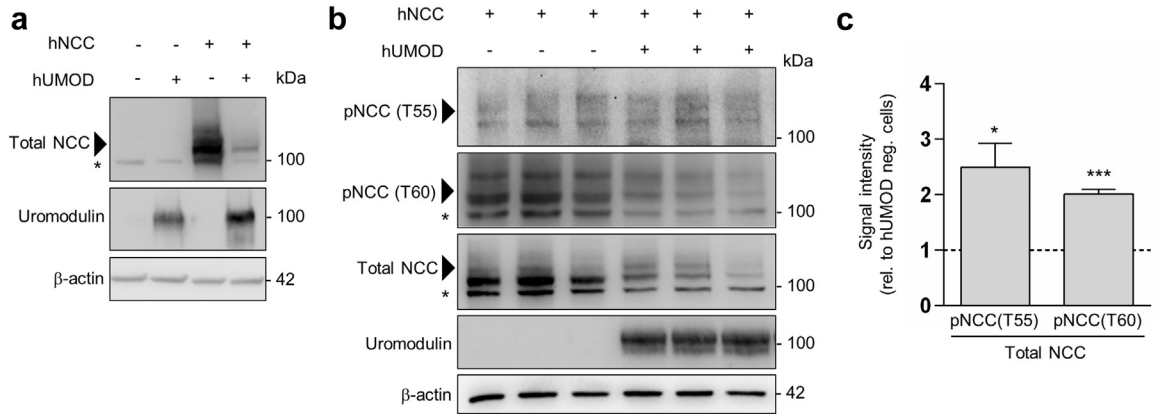

Figure 8 | Uromodulin facilitates Na^+/Cl^- cotransporter (NCC) phosphorylation *in vitro*. (**a**) Representative Western blot analysis for total NCC and uromodulin in whole cell lysates from human embryonic kidney (HEK) cells stably expressing human uromodulin (hUMOD) or control non–hUMOD-expressing HEK cells, either transiently transfected with human NCC (hNCC, 3 days after transfection) or mock-transfected, as indicated. β-actin is shown as a loading control. *Aspecific band at ~100 kDa, also identified in control cells that are mock-transfected and thus do not express hNCC. (**b**) Western blot analysis for T55 (corresponding to murine T53) phosphorylated NCC (pNCC), T60 (corresponding to mouse T58) pNCC, total NCC, and uromodulin in total cell lysates from hUMOD-expressing HEK cells and control non–hUMOD-expressing HEK cells transiently transfected with human NCC (hNCC). β-actin is shown as a loading control. *Aspecific band. (**c**) Quantification of Western blot signal intensity ratios of pNCC (T55 and T60) over total NCC in hUMOD-expressing HEK cells relative to control non–hUMOD-expressing HEK cells. Bars indicate average ± SEM. Unpaired 2-tailed *t* test, hUMOD-expressing cells versus control HEK cells: *$P < 0.05$; ***$P < 0.001$. To optimize viewing of this image, please see the online version of this article at www.kidney-international.org.

and thiazide testing are unable to discriminate between compensatory mechanisms due to chronic TAL dysfunction and direct consequences of uromodulin deficiency in DCT. The chronic inactivation of NKCC2 by furosemide infusion not only eliminates any difference in NKCC2 activity but also tests the ability of the DCT to compensate for increased distal delivery of NaCl and divalent cations. Using this test combined with immunofluorescence quantification, we could demonstrate for the first time that uromodulin activates NCC in the DCT1, a role that is reflected by sodium wasting and a blunted response to HCTZ and a defective ability to compensate renal Ca^{2+} losses in *Umod*$^{-/-}$ mice.

The mechanism by which uromodulin regulates NCC activation is unclear and will require dedicated *in vitro* investigations. On the basis of the close homology between the cotransporters,[38] one could hypothesize that mechanisms similar to those reported for NKCC2 could operate. It is currently unclear how uromodulin modulates the activity of NKCC2; previous studies incriminated the SPAK/OSR1 pathway,[15] tumor necrosis factor-α signaling,[14] or modulations of intracellular Cl^- levels.[12] Alternatively, luminal uromodulin might stabilize NCC in its activated form in the DCT1, in absence of intracellular effects, as was previously reported for TRPV5.[39] However, this would not explain the redistribution of phosphorylated NCC toward more distal DCT segments and the increased pNCC levels that are found in *Umod*$^{-/-}$ mice at baseline. Our results suggesting that uromodulin facilitates NCC phosphorylation in stably transfected HEK cells support a cell-autonomous mechanism involving posttranslational modifications rather than transcriptional changes in *Slc12a3*. The evidence of strongly reduced pSPAK/pOSR1 levels in the DCT1 of *Umod*$^{-/-}$ mice suggests a possible involvement of the WNK-SPAK/OSR1 pathway in this local regulation.

Regarding the inappropriate urinary Ca^{2+} losses in *Umod*$^{-/-}$ mice under furosemide, we detected no differences in TRPV5 expression in *Umod*$^{+/+}$ and *Umod*$^{-/-}$ kidneys, ruling out a problem of apical Ca^{2+} entry. Instead, the urine Ca^{2+} losses could be due to the shift of NaCl reabsorption to DCT2 segments, responsible for Ca^{2+} uptake. In this setting, the basolateral Na^+/Ca^{2+} exchanger NCX might function as Na^+ export system, thus increasing intracellular Ca^{2+} levels and impairing Ca^{2+} uptake in DCT2. This hypothesis is supported by the fact that the hypercalciuria of furosemide-infused *Umod*$^{-/-}$ mice was no longer in evidence after HCTZ administration. The hypercalciuria that is observed in pseudohypoaldosteronism type II patients with constitutive activation of NCC could be mediated by similar mechanisms.[40]

The demonstration that uromodulin regulates NCC in the DCT, together with the previously described effect on NKCC2,[12,15] entails potential clinical implications. Both NKCC2 and NCC are involved in recessive genetic disorders leading to salt wasting and hypotension,[41] whereas the carrier status of loss-of-functions mutations in either *SLC12A1* or *SLC12A3* is associated with reduced blood pressure in the population.[42] The expression levels of uromodulin directly affect blood pressure control in mice, via NKCC2-mediated NaCl handling in the TAL.[14,15] In humans, common variants in the *UMOD* promoter that are associated with reduced expression of uromodulin were associated with a reduced risk for arterial hypertension and cardiovascular events.[10] Conversely, carriers of *UMOD* promoter variants driving higher uromodulin expression are more responsive to

furosemide treatment in terms of natriuresis and blood pressure decrease.[15] Our findings raise questions regarding the role of uromodulin in NCC-mediated NaCl and blood pressure control and the modulation of thiazide response. The altered Ca^{2+} handling in *Umod*$^{-/-}$ mice suggests a role for uromodulin in Ca^{2+} homeostasis, also supported by the independent association of uromodulin excretion with urinary Ca^{2+} excretion in population cohorts.[43]

Converging studies indicate a substantial plasticity of the DCT. Increased distal NaCl delivery induced by chronic furosemide treatment was followed by an expansion of the DCT area in rats,[33] whereas genetic deletion of NCC resulted in marked hypoplasia of the early DCT.[44] Elegant studies by Lalioti *et al.*[45] demonstrated that the DCT plasticity was essentially driven by the activity of NCC, with corresponding alterations in electrolyte and blood pressure control. The DCT hypertrophy observed in rats was shown to be related to increased DNA synthesis and cellular proliferation,[46] but precise mechanisms underlying this plasticity remain unknown. Our data support a role for uromodulin in the functional heterogeneity along the DCT: *Umod*$^{-/-}$ mice show less pNCC in DCT1 and increased pNCC in DCT2, paralleled by an expansion of DCT2. When exposed to chronic distal salt loading (furosemide), *Umod*$^{-/-}$ mice show a severely blunted capacity to increase NCC phosphorylation and lack the capacity to upregulate the DCT1 and DCT2 areas, compared with *Umod*$^{+/+}$ mice. Whether these structural changes result from the lack of uromodulin acting as a trophic factor for the DCT1 or reflect changes in NCC activity requires further investigations.

In conclusion, our studies uncover a new role for uromodulin, in a new kidney tubular segment. In view of the central homeostatic role of the DCT, intriguing questions include the potential contribution of the DCT in the association of *UMOD* variants with chronic kidney disease and hypertension and in rare diseases caused by mutations in *UMOD*.

MATERIALS AND METHODS

Animals

For expression analysis, 8–12-week-old C57BL6J male mice purchased from Charles River (L'Arbresle, France), mice expressing EGFP under the control of *Pvalb* gene promoter,[27,28] and mice heterozygous for the C125R *Umod* mutation[7] were used. *Umod*$^{+/+}$ and *Umod*$^{-/-}$ mice (FVB background) were used for metabolic studies. All mice were maintained in 12-hour light–dark cycles with *ad libitum* water and standard laboratory diet before experiments. For chronic NKCC2 inhibition, mice were anesthetized with isoflurane (3%–5% in oxygen) and osmotic mini-pumps 2001 (Alzet, Palo Alto, CA), filled with furosemide (Sigma, St. Louis, MO) (75 μg/g body weight [gBW]/d) dissolved in 50% dimethylsulfoxide/0.9% NaCl (pH 8.0) were subcutaneously inserted in the interscapular region. Osmotic pumps were incubated overnight at 37°C in 0.9% NaCl solution before implantation. All animal experiments were performed in accordance with the ethical guidelines at the University of Zurich and the legislation of animal care and experimentation of Canton Zurich, Switzerland (ZH049/17).

Metabolic studies

Mice were individually housed in metabolic cages (UNO BV, Zevenaar, The Netherlands) with *ad libitum* drinking water and powder food. Overnight urine collection (16 hours) was performed after 2 sessions of adaptation. To evaluate the response to NCC inhibition, urine excreted during 6 hours after an i.p. bolus injection of HCTZ (50 μg/gBW; Sigma) was collected and compared with urine excreted during the same timescale after injection of vehicle (0.9 % NaCl, 10 μl/gBW). HCTZ was dissolved in 0.9% NaCl, and 10 μl per gBW was injected for each mouse. Urine samples were centrifuged and stored at −20°C until analysis. At the end of the experiment, mice were deeply anesthetized with an i.p. injection of ketamine (100 mg/kg BW; Streuli Pharma AG, Uznach, Switzerland)/xylasine (20 mg/kg BW; Streuli Pharma AG), and blood was obtained from the inferior vena cava. Mice were then killed by cervical dislocation for organ collection. Harvested tissue was snap-frozen in liquid nitrogen and kept at −80°C. Blood samples were centrifuged for 20 minutes at 2000 × *g*, and serum was separated and stored at −20°C.

Urine and blood chemistry

Urinary and serum Na^+ and K^+ concentrations were determined by flame photometer. Urinary and serum Ca^{2+}, Mg^{2+}, Cl^-, and creatinine concentrations were measured with a UniCel DxC 800 Synchron Clinical System (Beckman Coulter, Analis, sa/nv, Villepinte, France) and an i-STAT analyzer (Abbott Diagnostics, Maidenhead, UK). Urine osmolality was measured by Osmometer (Fiske, Needham Heights, MA).

Microdissection of renal tubules

Mouse kidneys were briefly digested with type 2 collagenase as previously described.[25] Renal tubules were isolated manually according to morphologic criteria and were lysed in the RNA lysis buffer from the RNAqueous Total RNA Isolation Kit (Invitrogen, Carlsbad, CA). Quantitative reverse transcription–polymerase chain reaction was performed on pools of 70 TALs isolated as previously described.[25] When required, tweezer-assisted microdissection on collagenase-perfused kidneys from C57BL/6J mice was performed, to collect mTAL and cTAL enriched fractions.[47]

Gene expression analysis

Total RNA was extracted from isolated renal tubules with the RNAqueous Total RNA Isolation Kit (Invitrogen) according to the manufacturer's protocol. DNAse I treatment was performed to eliminate genomic DNA contamination. One microgram of RNA was used to perform the reverse transcriptase reaction with the iScript cDNA Synthesis Kit (Bio-Rad Laboratories, Hercules, CA). Changes in target genes mRNA levels were determined by relative RT-qPCR with a CFX96 Real-Time PCR Detection System (Bio-Rad Laboratories) using iQ SYBR Green Supermix (Bio-Rad Laboratories) detection of single PCR product accumulation. RT-qPCR analyses were performed in duplicate with 100 nM of both sense and antisense primers in a final volume of 20 μl using iQ SYBR Green Supermix (Bio-Rad Laboratories). Specific primers were designed using Primer3 (Supplementary Table S2).[48] PCR conditions were 95°C for 3 minutes, followed by 40 cycles of 15 seconds at 95°C and 30 seconds at 60°C. The PCR products were sequenced with the BigDye terminator kit (Perkin Elmer Applied Biosystems, Foster City, CA). The multiScreen SEQ_{384} Filter Plate (Millipore, Billerica, MA) and Sephadex G-50 DNA Grade Fine (Amersham Biosciences, Piscataway, NJ) dye terminator removal were used to purify

sequences reactions before analysis on an ABI3100 capillary sequencer (Perkin Elmer Applied Biosystems).

In situ hybridization

We used RNAscope Assays (ACD Advanced Cell Diagnostics Srl, Hayward, CA) to visualize single RNA molecules per cell in 10–20-µm cryo-sections of the mouse kidney fixed with 4% paraformaldehyde. Sections were incubated with Probe-C3 for *Umod* (20ZZ probe targeting mouse Umod, position 221-1039 of NM_009470.5), Probe-C2 for *Slc12a1* (20ZZ probe targeting mouse Slc12a1, position 1050-2083 of NM_183354.2), and Probe-C1 for *Slc12a3* (20ZZ probe targeting mouse Slc12a3, position 516-1369 of NM_001205311.1). Images were obtained with confocal microscope SP8 (Leica Microsystems, Wetzlar, Germany).

Cellular expression studies

HEK293 (ATCC, LGC Standards, Wesel, Germany) and HEK cells stably expressing hUMOD (gift from L. Rampoldi[35]) were used. HEK293 and hUMOD-expressing HEK cells were maintained in Dulbecco's modified Eagle's medium high glucose with sodium pyruvate and glutamine (Life Technologies, Gaithersburg, MD) supplemented with fetal bovine serum (10%) and antibiotics (100 µg/ml streptomycin and 100 U/ml penicillin). The cells were grown at 37°C, 5% CO_2. Both cell lines were transfected with plasmid expressing human SLC12A3 (NCC), EX-Z2925-M02 (GeneCopoeia, Rockville, MD). Cells were placed in 450 µl of Dulbecco's modified Eagle's medium, and 50 µl of polyplex (JetPEI DNA transfection reagent; Polyplus, New York, NY) solution containing 0.5 µg of SLC12A3 plasmid was added to the cells. Subsequent to overnight incubation with the plasmid, the media was replaced with 0.5 ml of complete Dulbecco's modified Eagle's medium, and cells were used 72 hours after transfection.

Western blot analysis

Membrane fraction protein was enriched from kidney samples as described previously.[49] HEK cells were lysed in radioimmunoprecipitation assay buffer supplemented with protease and phosphatase inhibitors (Roche, Basel, Switzerland) to obtain total proteins. Samples were mixed with the Laemmli buffer containing dithiothreitol. Forty to fifty micrograms of protein were loaded for sodium dodecylsulfate–polyacrylamide gel electrophoresis and transferred to polyvinylidene diflouride membranes. Then, membranes were blocked with 5% skim milk or 3% bovine serum albumin in tris-buffered saline and incubated with rabbit anti-NCC (1:1000; Millipore), -pT53 or pT58 NCC (1:5000, previously characterized[50]), rabbit anti-phospho SPAK (Ser373)/phospho OSR1 (Ser325) (07-2273, 1:500; Millipore), rabbit anti-SPAK (07-2271, 1:1000; Millipore), or rabbit anti-OSR1 (07-2264, 1:500; Millipore) antibody overnight at 4°C. Membrane was washed with tris-buffered saline and incubated with horseradish peroxidase–conjugated rabbit IgG (1:10000; Dako, Carpinteria, CA), and signals were revealed with the ChemiDoc imaging system (Bio-Rad Laboratories). The protein expression was normalized with the signal obtained with flottilin-1 or β-actin expression.

Immunofluorescent analysis

Left kidneys were perfused and fixed with 4% paraformaldehyde/phosphate-buffered saline and processed in paraffin. Four-micrometer-thick paraffin sections were heated at 95°C for 10 minutes in 10 mM Na-citrate (pH 6.0) for antigen retrieval and followed by a blocking step with a solution containing 3% bovine serum albumin, 0.05% Tween-20, 50 mM glycine, and 50 mM NH_4Cl in phosphate-buffered saline. Then sections were incubated with sheep anti-uromodulin (1:500; Meridian, Memphis, TN), rabbit anti-NCC (1:500; Millipore), pT53 NCC (1:1000, previously characterized[50]), TRPV5 (1:500, a gift from O. Bonny), phospho SPAK (Ser373)/phospho OSR1 (Ser325)(07-2273, 1:300; Millipore), or mouse anti-parvalbumin (1:500; Swant, Marly, Switzerland) antibodies, overnight at 4 °C. After washing steps, sections were incubated with fluorescein-conjugated secondary antibodies (1:500; Invitrogen) for 1 hour at room temperature. Sections were mounted in ProLong Gold antifade mounting medium (Invitrogen), and images were aquired with a confocal microscope (Leica SP5 or SP8).

Quantification of fluorescence intensity and renal fractional volume

Quantification of T53 pNCC immunofluorescent intensity was perfomed on kidney sections costained for T53 pNCC and parvalbumin to distinguish between DCT1 (T53 pNCC-positive; parvalbumin-positive) and DCT2 (T53 pNCC-positive; parvalbumin-negative). A series of pictures (at least 5) from at least 3 different mice were acquired using a confocal microscope (Leica Microsystems) and a ×40 oil immersion objective, with parameters kept unchanged. Using ImageJ software,[51] a threshold was set to select all the stained area, and all T53 pNCC-positive tubules were outlined, assigned as DCT1 or DCT2. The intensity of each tubule was calculated from division of integrated signal density within the tubule by tubular area. Tubules at the border of the picture were excluded.[34]

Renal fractional volume occupied by DCT1 and DCT2 was assessed in the same T53 pNCC/parvalbumin costained kidney sections. A series of low-magnification pictures (6–9) from at least 2 different mice was acquired using a confocal microscope (Leica Microsystems) and a ×10 objective, with parameters kept unchanged. Using ImageJ software,[51] all T53 pNCC-positive tubules were outlined, assigned as DCT1 or DCT2, and their combined area quantified. Then the area of the corresponding total kidney section was determined and used as a normalization factor.[34]

Statistics

Data are presented as means ± SEM. Two-tailed unpaired and paired Student's *t* tests were used for statistical analysis, as indicated, and a *P* value of <0.05 was considered significant.

DISCLOSURE

All the authors declared no competing interests.

ACKNOWLEDGMENTS

We thank Prof. Olivier Bonny (University of Lausanne), Prof. Rajesh Thakker (University of Oxford), and Prof. Luca Rampoldi (San Raffaele Scientific Institute, Milan) for material and discussions; Dr. Dominique Loffing-Cueni for expert scientific assistance; and Huguette Debaix, Nadine Gölz, Nadine Nägele, Yvette Cnops, Guglielmo Schiano, Jan Czogalla, and Monique Carrel for excellent technical assistance and discussion. These studies were supported by an Advanced Postdoc Mobility Fellowship from the Swiss National Science Foundation (P300P3_158521) and Forschungskredit Postdoc from the University of Zürich (to NT); the Fonds National de la Recherche, Luxembourg (6903109) and University Research Priority Programme "Integrative Human Physiology, ZIHP" of the University of Zurich (to EGO); the Swiss National Centre of Competence in Research Kidney Control of Homeostasis (NCCR Kidney.CH) program, the Swiss National Science Foundation (31003A_169850), and the Rare Disease Initiative Zürich

(Radiz), a clinical research priority program of the University of Zurich, Switzerland (to OD).

SUPPLEMENTARY MATERIAL

Figure S1. *Umod* transcripts in public databases.
Figure S2. Validation of *Umod in situ* hybridization probe.
Figure S3. Representative low-magnification picture for measurement of distal convoluted tubule areas.
Figure S4. Structural adaptations in late distal convoluted tubule-2 segments in $Umod^{+/+}$ and $Umod^{-/-}$ mice.
Figure S5. Sodium and calcium wasting in $Umod^{-/-}$ mice after furosemide infusion.
Figure S6. Reduced pSPAK/pOSR1 levels in the early distal convoluted tubule-1 of $Umod^{-/-}$ kidneys.
Table S1. Plasma parameters after chronic furosemide infusion.
Table S2. List of primers for quantitative polymerase chain reaction analysis.
Supplementary material is linked to the online version of the paper at www.kidney-international.org.

REFERENCES

1. Pennica D, Kohr WJ, Kuang WJ, et al. Identification of human uromodulin as the Tamm-Horsfall urinary glycoprotein. *Science*. 1987;236:83–88.
2. Uhlen M, Fagerberg L, Hallstrom BM, et al. Proteomics. Tissue-based map of the human proteome. *Science*. 2015;347:1260419.
3. Bachmann S, Metzger R, Bunnemann B. Tamm-Horsfall protein-mRNA synthesis is localized to the thick ascending limb of Henle's loop in rat kidney. *Histochemistry*. 1990;94:517–523.
4. Sikri KL, Foster CL, MacHugh N, Marshall RD. Localization of Tamm-Horsfall glycoprotein in the human kidney using immuno-fluorescence and immuno-electron microscopical techniques. *J Anat*. 1981;132:597–605.
5. Devuyst O, Olinger E, Rampoldi L. Uromodulin: from physiology to rare and complex kidney disorders. *Nat Rev Nephrol*. 2017;13:525–544.
6. Eckardt KU, Alper SL, Antignac C, et al. Autosomal dominant tubulointerstitial kidney disease: diagnosis, classification, and management–A KDIGO consensus report. *Kidney Int*. 2015;88:676–683.
7. Piret SE, Olinger E, Reed AA, et al. Mouse model for inherited renal fibrosis associated with endoplasmic reticulum stress. *Dis Model Mech*. 2017;10:773–786.
8. Pattaro C, Teumer A, Gorski M, et al. Genetic associations at 53 loci highlight cell types and biological pathways relevant for kidney function. *Nat Commun*. 2016;7:10023.
9. Gudbjartsson DF, Holm H, Indridason OS, et al. Association of variants at UMOD with chronic kidney disease and kidney stones-role of age and comorbid diseases. *PLoS Genet*. 2010;6:e1001039.
10. Padmanabhan S, Melander O, Johnson T, et al. Genome-wide association study of blood pressure extremes identifies variant near UMOD associated with hypertension. *PLoS Genet*. 2010;6:e1001177.
11. Mo L, Huang HY, Zhu XH, et al. Tamm-Horsfall protein is a critical renal defense factor protecting against calcium oxalate crystal formation. *Kidney Int*. 2004;66:1159–1166.
12. Mutig K, Kahl T, Saritas T, et al. Activation of the bumetanide-sensitive Na+,K+,2Cl- cotransporter (NKCC2) is facilitated by Tamm-Horsfall protein in a chloride-sensitive manner. *J Biol Chem*. 2011;286:30200–30210.
13. Renigunta A, Renigunta V, Saritas T, et al. Tamm-Horsfall glycoprotein interacts with renal outer medullary potassium channel ROMK2 and regulates its function. *J Biol Chem*. 2011;286:2224–2235.
14. Graham LA, Padmanabhan S, Fraser NJ, et al. Validation of uromodulin as a candidate gene for human essential hypertension. *Hypertension*. 2014;63:551–558.
15. Trudu M, Janas S, Lanzani C, et al. Common noncoding UMOD gene variants induce salt-sensitive hypertension and kidney damage by increasing uromodulin expression. *Nat Med*. 2013;19:1655–1660.
16. Hoyer JR, Sisson SP, Vernier RL. Tamm-Horsfall glycoprotein: ultrastructural immunoperoxidase localization in rat kidney. *Lab Invest*. 1979;41:168–173.
17. Bachmann S, Koeppen-Hagemann I, Kriz W. Ultrastructural localization of Tamm-Horsfall glycoprotein (THP) in rat kidney as revealed by protein A-gold immunocytochemistry. *Histochemistry*. 1985;83:531–538.
18. Sikri KL, Foster CL, Bloomfield FJ, Marshall RD. Localization by immunofluorescence and by light- and electron-microscopic immunoperoxidase techniques of Tamm-Horsfall glycoprotein in adult hamster kidney. *Biochem J*. 1979;181:525–532.
19. Sikri KL, Alexander DP, Foster CL. Localization of Tamm-Horsfall glycoprotein in the normal rat kidney and the effect of adrenalectomy on its localization in the hamster and rat kidney. *J Anat*. 1982;135:29–45.
20. de Baaij JH, Groot Koerkamp MJ, Lavrijsen M, et al. Elucidation of the distal convoluted tubule transcriptome identifies new candidate genes involved in renal Mg(2+) handling. *Am J Physiol Renal Physiol*. 2013;305:F1563–F1573.
21. Peach RJ, Day WA, Ellingsen PJ, McGiven AR. Ultrastructural localization of Tamm-Horsfall protein in human kidney using immunogold electron microscopy. *Histochem J*. 1988;20:156–164.
22. Cheval L, Pierrat F, Dossat C, et al. Atlas of gene expression in the mouse kidney: new features of glomerular parietal cells. *Physiol Genomics*. 2011;43:161–173.
23. Lee JW, Chou CL, Knepper MA. Deep sequencing in microdissected renal tubules identifies nephron segment-specific transcriptomes. *J Am Soc Nephrol*. 2015;26:2669–2677.
24. Chabardes-Garonne D, Mejean A, Aude JC, et al. A panoramic view of gene expression in the human kidney. *Proc Natl Acad Sci U S A*. 2003;100:13710–13715.
25. Glaudemans B, Terryn S, Golz N, et al. A primary culture system of mouse thick ascending limb cells with preserved function and uromodulin processing. *Pflugers Arch*. 2014;466:343–356.
26. Castrop H, Schnermann J. Isoforms of renal Na-K-2Cl cotransporter NKCC2: expression and functional significance. *Am J Physiol Renal Physiol*. 2008;295:F859–F866.
27. Meyer AH, Katona I, Blatow M, et al. In vivo labeling of parvalbumin-positive interneurons and analysis of electrical coupling in identified neurons. *J Neurosci*. 2002;22:7055–7064.
28. Picard N, Trompf K, Yang CL, et al. Protein phosphatase 1 inhibitor-1 deficiency reduces phosphorylation of renal NaCl cotransporter and causes arterial hypotension. *J Am Soc Nephrol*. 2014;25:511–522.
29. Wang F, Flanagan J, Su N, et al. RNAscope: a novel in situ RNA analysis platform for formalin-fixed, paraffin-embedded tissues. *J Mol Diagn*. 2012;14:22–29.
30. Bleich M, Wulfmeyer VC, Himmerkus N, Milatz S. Heterogeneity of tight junctions in the thick ascending limb. *Ann N Y Acad Sci*. 2017;1405:5–15.
31. Subramanya AR, Ellison DH. Distal convoluted tubule. *Clin J Am Soc Nephrol*. 2014;9:2147–2163.
32. Loffing J, Loffing-Cueni D, Valderrabano V, et al. Distribution of transcellular calcium and sodium transport pathways along mouse distal nephron. *Am J Physiol Renal Physiol*. 2001;281:F1021–F1027.
33. Kaissling B, Bachmann S, Kriz W. Structural adaptation of the distal convoluted tubule to prolonged furosemide treatment. *Am J Physiol*. 1985;248:F374–F381.
34. Jensen EC. Quantitative analysis of histological staining and fluorescence using ImageJ. *Anat Rec (Hoboken)*. 2013;296:378–381.
35. Schaeffer C, Santambrogio S, Perucca S, et al. Analysis of uromodulin polymerization provides new insights into the mechanisms regulating ZP domain-mediated protein assembly. *Mol Biol Cell*. 2009;20:589–599.
36. Richardson C, Rafiqi FH, Karlsson HK, et al. Activation of the thiazide-sensitive Na+-Cl- cotransporter by the WNK-regulated kinases SPAK and OSR1. *J Cell Sci*. 2008;121:675–684.
37. Wiggins RC. Uromucoid (Tamm-Horsfall glycoprotein) forms different polymeric arrangements on a filter surface under different physicochemical conditions. *Clin Chim Acta*. 1987;162:329–340.
38. Bazua-Valenti S, Castaneda-Bueno M, Gamba G. Physiological role of SLC12 family members in the kidney. *Am J Physiol Renal Physiol*. 2016;311:F131–F144.
39. Wolf MT, Wu XR, Huang CL. Uromodulin upregulates TRPV5 by impairing caveolin-mediated endocytosis. *Kidney Int*. 2013;84:130–137.
40. Yang SS, Hsu YJ, Chiga M, et al. Mechanisms for hypercalciuria in pseudohypoaldosteronism type II-causing WNK4 knock-in mice. *Endocrinology*. 2010;151:1829–1836.
41. Seyberth HW, Schlingmann KP. Bartter- and Gitelman-like syndromes: salt-losing tubulopathies with loop or DCT defects. *Pediatr Nephrol*. 2011;26:1789–1802.

42. Ji W, Foo JN, O'Roak BJ, et al. Rare independent mutations in renal salt handling genes contribute to blood pressure variation. *Nat Genet*. 2008;40:592–599.
43. Pruijm M, Ponte B, Ackermann D, et al. Associations of urinary uromodulin with clinical characteristics and markers of tubular function in the general population. *Clin J Am Soc Nephrol*. 2016;11:70–80.
44. Loffing J, Vallon V, Loffing-Cueni D, et al. Altered renal distal tubule structure and renal Na(+) and Ca(2+) handling in a mouse model for Gitelman's syndrome. *J Am Soc Nephrol*. 2004;15:2276–2288.
45. Lalioti MD, Zhang J, Volkman HM, et al. Wnk4 controls blood pressure and potassium homeostasis via regulation of mass and activity of the distal convoluted tubule. *Nat Genet*. 2006;38:1124–1132.
46. Loffing J, Le Hir M, Kaissling B. Modulation of salt transport rate affects DNA synthesis in vivo in rat renal tubules. *Kidney Int*. 1995;47:1615–1623.
47. Morla L, Crambert G, Mordasini D, et al. Proteinase-activated receptor 2 stimulates Na,K-ATPase and sodium reabsorption in native kidney epithelium. *J Biol Chem*. 2008;283:28020–28028.
48. Rozen S, Skaletsky H. Primer3 on the WWW for general users and for biologist programmers. *Methods Mol Biol*. 2000;132:365–386.
49. Tokonami N, Cheval L, Monnay I, et al. Endothelin-1 mediates natriuresis but not polyuria during vitamin D-induced acute hypercalcaemia. *J Physiol*. 2017;595:2535–2550.
50. Sorensen MV, Grossmann S, Roesinger M, et al. Rapid dephosphorylation of the renal sodium chloride cotransporter in response to oral potassium intake in mice. *Kidney Int*. 2013;83:811–824.
51. Schneider CA, Rasband WS, Eliceiri KW. NIH Image to ImageJ: 25 years of image analysis. *Nat Methods*. 2012;9:671–675.